

Cite this: *J. Mater. Chem. A*, 2020, **8**, 278

## A 3D-printed ultra-high Se loading cathode for high energy density quasi-solid-state Li–Se batteries†

Xuejie Gao,<sup>‡,ab</sup> Xiaofei Yang,<sup>‡,a</sup> Sizhe Wang,<sup>a</sup> Qian Sun,<sup>a</sup> Changtai Zhao,<sup>a</sup> Xiaona Li,<sup>a</sup> Jianwen Liang,<sup>a</sup> Matthew Zheng,<sup>a</sup> Yang Zhao,<sup>a</sup> Jiwei Wang,<sup>ab</sup> Minsi Li,<sup>ab</sup> Ruing Li,<sup>a</sup> Tsun-Kong Sham<sup>\*b</sup> and Xueliang Sun<sup>†,a</sup>

Quasi-solid-state lithium–selenium batteries (QSSLSEBs) assembled with gel polymer electrolytes (GPEs) are a promising class of next-generation rechargeable batteries due to their safety, high energy density and shuttle-free charging/discharging process. Nevertheless, both poor Li<sup>+</sup> transport in thick electrodes and Li dendrite growth limit the improvements of the current density as well as Se loading, resulting in low energy/power densities. Herein, we proposed to combine a 3D-printed carbon nanotube (CNT) interlayer to protect the Li anode with a 3D-printed Se cathode (named 3DPSe) filled with GPEs in high Se loading cathodes to achieve ultra-high energy/power-density QSSLSEBs. Benefitting from the 3D-printed CNT interlayer in suppressing Li dendrite growth, the Li–Li symmetric cell stably runs for 400 h (3 mA cm<sup>-2</sup>; 3 mA h cm<sup>-2</sup>), which is almost one order of magnitude longer than the interlayer-free cell. Moreover, 3DPSe acts as a host for GPE impregnation to fabricate interconnect Li<sup>+</sup> transport channels in the thick Se cathode, enabling fast Li<sup>+</sup> transport. Accordingly, the QSSLSEB assembled with an ultra-high Se loading of 20 mg cm<sup>-2</sup> delivers the highest reported areal capacity of 12.99 mA h cm<sup>-2</sup> at 3 mA cm<sup>-2</sup>. This work is expected to open up promising opportunities to develop other high-energy/power-density solid-state lithium batteries (SSLBs).

Received 26th September 2019

Accepted 15th November 2019

DOI: 10.1039/c9ta10623e

rsc.li/materials-a

## Introduction

The increasing demands of portable electronic devices and electric vehicles have largely placed emphasis on developing high-energy-density rechargeable batteries.<sup>1–5</sup> Since CMK-3 was reported as a sulfur host, lithium–sulfur (Li–S) batteries have received great attention due to their high theoretical gravimetric energy density (2570 W h kg<sup>-1</sup>), which is 3–5 times that of the state-of-the-art Li-ion batteries.<sup>6–8</sup> Nevertheless, Li–S batteries are still confronted with several issues preventing their practical applications such as the low conductivity of sulfur (5 × 10<sup>-28</sup> S m<sup>-1</sup>) and the “shuttle effect” caused by the high solubility of polysulfides.<sup>9–12</sup> Tremendous efforts have been focused on solving the aforementioned issues, but a solution is yet to be found for large-scale practical production and commercialization. Accordingly, some researchers also explore lithium–selenium (Li–Se) batteries, because selenium (Se) is an element in the same main group as S in the periodic table.<sup>13–15</sup> Compared with S, Se, a semiconductor, shows a higher electronic conductivity of 1 × 10<sup>-5</sup> S m<sup>-1</sup>, 10<sup>22</sup> higher than that of S,

enabling Li–Se batteries with high electrochemical kinetics. Moreover, Li–Se batteries possess comparable volumetric capacity to Li–S (3253 mA h cm<sup>-3</sup> vs. 3467 mA h cm<sup>-3</sup>).<sup>16,17</sup> More importantly, it has been widely accepted that Li–Se batteries undergo a solid-state lithiation process, a polyselenide-free process in a carbonate electrolyte.<sup>15,18</sup> In other words, there is no “shuttle effect” during the charging/discharging process, contributing to a high utilization of Se and prolonged cycling life.<sup>15</sup> Therefore, Li–Se batteries show promising applications as next-generation rechargeable batteries.

In the last few years, most of the achievements made in Li–Se batteries are based on liquid electrolyte systems.<sup>19–22</sup> Issues like leakage, flammability and electrochemical instability of liquid electrolytes have triggered safety issues as well as restrictions on the practical application of Li–Se batteries.<sup>23</sup> Hence, solid-state lithium batteries (SSLBs), replacing liquid electrolytes with high-stability and inflammable solid-state electrolytes (SSEs), have been regarded as a good choice for further application in terms of safety.<sup>24–26</sup> Recently, our group developed an all-solid-state Li–Se battery (denoted as ASSLSEB) with sulfide-based SSEs and had achieved excellent cycling stability with a capacity retention of 90% within 100 cycles.<sup>27</sup> However, the relatively low ionic conductivity of Li<sub>3</sub>PS<sub>4</sub> (3 × 10<sup>-4</sup> S cm<sup>-1</sup>) limited the improvement of the current density (50 mA g<sup>-1</sup>) as did the Se loading (3 mg cm<sup>-2</sup>), both of which cannot meet the requirements of high-energy/power-density SSLSEBs.<sup>28</sup> Thus,

<sup>a</sup>Department of Mechanical and Materials Engineering, University of Western Ontario, London, ON, N6A 5B9, Canada. E-mail: xsun9@uwo.ca

<sup>b</sup>Department of Chemistry, University of Western Ontario, London, ON, Canada

† Electronic supplementary information (ESI) available. See DOI: 10.1039/c9ta10623e

‡ These authors contributed equally to this work.

further exploration of higher ionic conductive SSEs combined with higher loading Se cathodes, in addition to operating the SSLSEB at a reasonable current density, is of significance. Gel polymer electrolytes (GPEs), a class of quasi-SSEs, exhibit high ionic conductivities and excellent wetting capabilities, and are able to reduce the interfacial resistance.<sup>29–31</sup> Moreover, GPEs show high flexibility, availability, scalability, and high safety, showing promising properties that enable QSSLSEBs to be operated at reasonable current densities with high Se loadings. Despite their fantastic properties, the poor mechanical strength that cannot effectively suppress the Li dendrite growth should be addressed when combining them with high Se loadings and operating at high current densities.<sup>30,32</sup>

Herein, an ultra-high-energy/power density QSSLSEB was realized by combining a 3D-printed CNT interlayer with high Se-loading GPE-filled cathodes. Thanks to the 3D-printed CNT interlayer in suppressing Li dendrite growth, the Li–Li symmetric cell stably runs for 400 h ( $3 \text{ mA cm}^{-2}$ ,  $3 \text{ mA h cm}^{-2}$ ). Furthermore, high Se loading cathodes with Se loadings of  $4\text{--}20 \text{ mg cm}^{-2}$  are realized by the 3D-printing technique based on the layer-by-layer structure.<sup>33–37</sup> The as-prepared 3D printed Se cathodes are henceforth labeled 3DPSe-*x*, where *x* is the Se loading. To facilitate the  $\text{Li}^+$  transport in the thick electrodes, a high ionic conductive GPE with an ionic conductivity of  $2.8 \times 10^{-3} \text{ S cm}^{-1}$  is impregnated into the 3D-printed grid structure to fabricate the interconnected  $\text{Li}^+$  transport channels. Benefitting from the high ionic conductivity of the GPE, interconnected  $\text{Li}^+$  transport channels built in the thick Se cathodes, and the lithium anode protection by the CNT interlayer, the QSSLSEBs delivered a highest reported areal capacity of  $12.99 \text{ mA h cm}^{-2}$  for the 3DPSe-20 cathode at a high current density of  $3 \text{ mA cm}^{-2}$ . More importantly, 3DPSe-4 exhibits excellent rate performance and delivers a high capacity of  $\sim 400 \text{ mA h g}^{-1}$  at a high current density of  $10 \text{ mA cm}^{-2}$ . This study opens a new window for high-energy/power-density SSLBs with high active material loadings *via* 3D printing, which will shed light on the development of other SSLBs such as Li-ion, Li–S, and Li–O<sub>2</sub> batteries.

## Experimental

### Synthesis of Se/C composites

Se powder and the BP-2000 carbon material with a weight ratio of 5 : 5 were mixed together and then put into a mortar for grinding for 30 min. After that, the mixture was heated at  $260 \text{ }^\circ\text{C}$  for 12 h in a tube furnace under an Ar atmosphere. Then they were heated at  $350 \text{ }^\circ\text{C}$  for 3 h to remove residual Se on the surface of the composite to achieve Se/C composites. After cooling to room temperature, the final Se/BP-2000 composite with a Se content of 48.2 wt% was obtained.

### Synthesis of 3DPSe cathodes with different Se loadings

The printing process was performed using a custom-made 3D printer equipped with a 3-axis micropositioning stage based on a preprogrammed pattern procedure (FFF Delta 3D printer). The printing ink was fabricated by mixing Se/C, acetylene black (AB),

carbon nanotubes (CNTs, diameter of 40–60 nm and length of 2  $\mu\text{m}$ ) and sodium alginate at a weight ratio of 7 : 1 : 1 : 1 with additional DI water. This mixture was put into a mixer machine to stir for 1 h. After that, the ink was loaded into a 3 mL syringe and extruded through a 150  $\mu\text{m}$  diameter nozzle. During the printing process, the grid pattern was preprogrammed with an overall diameter of 1 cm, coupled with a printing speed of  $6 \text{ mm s}^{-1}$ . After printing, the printed Se/C cathode with different layers was firstly frozen in a refrigerator at  $-20 \text{ }^\circ\text{C}$  to keep a good structure, and then freeze dried for 24 h to remove water. Finally, 3DPSe-4 (Se loading:  $4 \text{ mg cm}^{-2}$ ), 3DPSe-10 (Se loading:  $10 \text{ mg cm}^{-2}$ ) and 3DPSe-20 (Se loading:  $20 \text{ mg cm}^{-2}$ ) were obtained with 2 layers, 5 layers and 10 layers, respectively.

### Fabrication of the CNT interlayer

Firstly, carbon nanotubes (CNTs, diameter of 40–60 nm and length of 2  $\mu\text{m}$ ) and PVDF-HFP (poly(vinylidene fluoride-co-hexafluoropropylene) with a weight ratio of 8.5 : 1.5 were mixed with *N,N*-dimethylformamide (DMF) to form an ink. The as-prepared CNT ink was then loaded into a 3 mL syringe and extruded through a 200  $\mu\text{m}$  diameter nozzle. The 3D-printed CNT interlayers (denoted as CNT) were printed by using a 3D printer with a dense layer, which was preloaded with a printing program with a diameter of 10 mm at a print motion speed of  $5 \text{ mm s}^{-1}$ . After printing, the CNT interlayer was put in a freeze drier for 24 h. Finally, a freestanding CNT was obtained – an interlayer that can effectively protect the Li anode during the lithiation and delithiation cycling process.

### Fabrication of BCSe cathodes

A blade-casting method was used to coat the Se/C slurry by using the same printing Se/C slurry on the surface of Al foil. The blade cast Se/C (denoted as BCSe) cathodes with Se loadings of  $4 \text{ mg cm}^{-2}$ ,  $10 \text{ mg cm}^{-2}$  and  $20 \text{ mg cm}^{-2}$  were obtained by controlling the thickness to 300  $\mu\text{m}$ , 750  $\mu\text{m}$  and 1500  $\mu\text{m}$ , respectively. After that, they were dried by freeze drying. Finally, BCSe-4, BCSe-10 and BCSe-20 were obtained as counterparts.

### Fabrication of the gel polymer

First, 6 g of PVDF-HFP was dispersed in 44 g DMF solution by stirring for 24 h to obtain 12% PVDF-HFP solution. Then 1.5 g of SiO<sub>2</sub> nanoparticles were added into the above solution by stirring for 24 h. After that, the obtained gel polymer was coated on a clean glass substrate by controlling the thickness to 150  $\mu\text{m}$ . Subsequently, the gel polymer was immersed in a water coagulation bath for 20 min (phase inversion process), and put into a freeze drier for 24 h. Finally, a freestanding gel polymer was obtained by cutting it into circular shapes (diameter: 16 mm).

### Fabrication of 3DPSe/gel-polymer electrolyte (3DPSe/GPE) composites

First, the prepared gel-polymer solution was added to a Teflon plate. And then 3DPSe-4, 3DPSe-10 and 3DPSe-20 were immersed into this solution for 30 min. After that, we immersed the Teflon plate in a water coagulation bath for 30 min and then

put the gel polymer in a freeze drier for 24 h. Finally, 3DPSe/gel-polymer electrolyte (named 3DPSe/GPE) composites were obtained by cutting it into circular shapes (diameter: 10 mm).

### Fabrication of the gel-polymer electrolyte (GPE)

The prepared gel polymer was immersed into the electrolyte [10% fluoroethylene carbonate (FEC) in 1.0 M LiPF<sub>6</sub> in EC/DEC = 50/50 (v/v) by volume] for 2 h. These membrane samples were taken out and wiped with filter paper. After that, they were dried in a glovebox for 2 h before use. The electrolyte uptake of the membranes can be obtained based on the weight difference between the dried gel-polymer and swollen gel-polymer electrolyte by using the equation as follow:

$$\text{Electrolyte uptake} = (W_{\text{wet}} - W_{\text{dry}})/W_{\text{dry}} \times 100\%$$

where  $W_{\text{wet}}$  and  $W_{\text{dry}}$  are the weight of the wet GPE and dry GP, respectively. Therefore, the electrolyte uptake of the gel polymer is  $(516 \text{ mg} - 148 \text{ mg})/148 \text{ mg} \times 100\% = 249\%$ .

### Characterization methods

The morphology of the samples was examined by using a Hitachi S4800 SEM operated at 15 eV. The X-ray diffraction (XRD) patterns of the samples were recorded at  $2\theta$  ranging from  $10^\circ$  to  $90^\circ$  on a Bruker AXS D8 Advance with Cu K $\alpha$  radiation ( $\lambda = 1.54178 \text{ \AA}$ ). The weight content of the Se/C composite was measured with TGA, which was carried out in a N<sub>2</sub> atmosphere in the range of 20 to 600 °C by using an SDT Q600 thermogravimetric analyzer (TGA instrument).

### Electrochemical measurements

The 3DPSe cathodes and BCSe cathodes with different Se loadings were assembled into CR2032 coin cells in an Ar-filled glovebox. The cathode and Li anode were separated by a GPE with and without CNT interlayer protection of Li metal, and the cells were named Li/CNT|GPE|3DPSe- $x$  and Li|GPE|3DPSe- $x$  with different Se loadings, respectively. The cycling performance of the assembled batteries was tested using a LAND battery testing station, by applying different currents.

Electrochemical impedance spectroscopy (EIS) was performed at open-circuit voltage in a frequency range of  $5.0 \times 10^5 \text{ Hz}$  to  $1.0 \times 10^{-2} \text{ Hz}$  on a versatile multichannel potentiostat 3/Z (VMP3). The charge–discharge tests were carried out using a LAND CT-2001A system with voltages between 0.8 V and 3 V at room temperature. Unless otherwise specified, the specific capacities reported in this work were calculated based on Se and the voltages vs. Li<sup>+</sup>/Li.

The cycling stability test: a symmetric cell was assembled in a CR 2032-type coin cell. The GPE was used as the electrolyte. And a bare Li metal electrode or CNT/Li composite electrode was used as the working electrode and the counter electrode. The cell was tested in a repeating discharge/charge process at a current density of  $1 \text{ mA cm}^{-2}$  and  $3 \text{ mA cm}^{-2}$  with an areal charge of  $1 \text{ mA h cm}^{-2}$  and  $3 \text{ mA h cm}^{-2}$ , respectively. The current density was based on the area of the electrodes. The

cycling stability of the anodes was evaluated according to the stability of voltage hysteresis.

## Results and discussion

Fig. 1 shows the scheme of a QSSLSEB based on the 3D-printed Se/C host filled with the GPE, where the GPE can facilitate Li<sup>+</sup> transport in the cathode. The Se/C composite was fabricated *via* a simple melt-diffusion method.<sup>38,39</sup> The X-ray diffraction (XRD) patterns in Fig. S1† and thermogravimetric analysis (TGA) curve in Fig. S2† confirm that Se is well confined in the pores of BP2000 and the Se content is around 50 wt%. After that, the Se/C composite, sodium alginate (SA), carbon nanotubes (CNTs), and acetylene black (AB) with a weight ratio of 7 : 1 : 1 : 1 are dispersed/dissolved into water to form an ink for 3D printing. The layer-by-layer deposition of the Se-loaded ink realized grid structured cathodes, named 3DPSe- $x$  ( $x$  is the Se loading, Fig. S3†).

Fig. 2 displays the printed structures and morphologies of the 3DPSe- $x$  cathodes with 2, 5 and 10 layers. Obviously, the distance between two neighboring filaments is about 250  $\mu\text{m}$ , which forms  $250 \times 250 \mu\text{m}^2$  square pores (Fig. 2a–c). These pores act as hosts for GPE impregnation, facilitating Li<sup>+</sup> transport in the 3DPSe- $x$  electrodes. In addition, the cross-sectional images of Fig. 2d–f demonstrates that the thickness of each layer is well controlled at around 150  $\mu\text{m}$ , corresponding to one printed layer with a Se loading of  $2 \text{ mg cm}^{-2}$ . In other words, the 2, 5, and 10 layers of 3DPSe- $x$  cathodes possess thicknesses of around 300  $\mu\text{m}$ , 750  $\mu\text{m}$  and 1500  $\mu\text{m}$ , corresponding to Se loadings of 4, 10 and  $20 \text{ mg cm}^{-2}$ , respectively. Obviously, the filaments are closely stacked to ensure fast electron transport in the thick electrodes. Fig. 2g–k show a higher magnification of the 3DPSe cathode (Fig. 2g) and corresponding EDS mappings (Fig. 2h–k), demonstrating uniform elemental distribution of C, Na, and Se. Before assembling cells, the 3DSe- $x$  cathodes were immersed in the GPE (Fig. S4a† and 4b) to create continuous Li<sup>+</sup> transport channels in the 3DPSe- $x$  electrode. The associated SEM images are shown in Fig. S4c–g.† It is evident that the GPE is uniformly distributed in the whole 3DPSe- $x$  cathode (Fig. S4c–

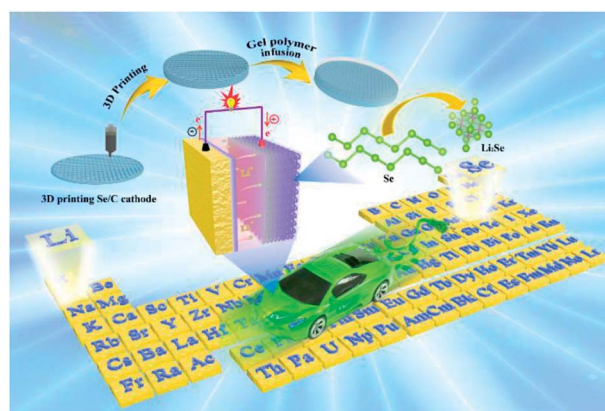


Fig. 1 Schematic of the design concept and fabrication process of the 3D-printed QSSLSEB.

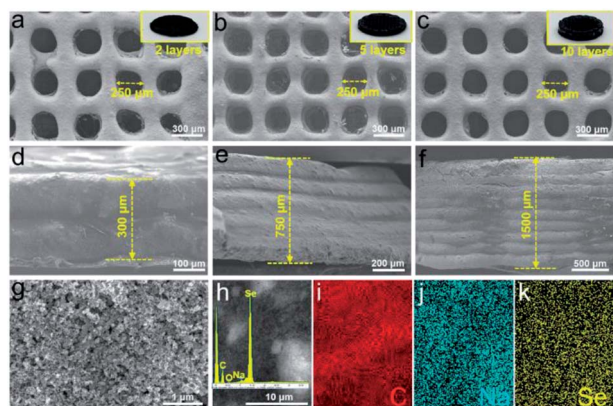


Fig. 2 Characterization of 3DPSe with 2, 5, and 10 layers. (a–c) Top view SEM images of (a) 3DPSe-4, (b) 3DPSe-10 and (c) 3DPSe-20 (4, 10, and 20 represent Se loading). The inset images show digital photographs of the corresponding printed Se/C cathode. (d–f) Cross sectional SEM images of (d) 3DPSe-4, (e) 3DPSe-10 and (f) 3DPSe-20. (g–k) SEM images with high magnification of the printed Se/C cathode and corresponding elemental EDS spectrum of C, Na and Se distribution.

g<sup>†</sup>), thus further ensuring fast Li<sup>+</sup> transport. To improve the safety of Li–Se batteries, a PVDF-HFP-based GPE was obtained by a phase inversion method and activated with a carbonate electrolyte.<sup>7,40</sup> The thickness of the gel polymer electrolytes was determined to be 164 μm (Fig. S5<sup>†</sup>). Benefitting from the high electrolyte uptake of 249%, the as-prepared GPE shows a high ionic conductivity of  $2.8 \times 10^{-3} \text{ S cm}^{-1}$  (Fig. S6<sup>†</sup>). Considering the fast Li<sup>+</sup>/e<sup>-</sup> transport in the 3DPSe-x electrode and the high ionic conductivity of the GPE, excellent electrochemical performance of the assembled QSSLSEBs can be expected.

To inhibit the GPE penetrated by the Li dendrite and to enhance the safety of the QSSLSEBs, a 3D-printed CNT interlayer (Fig. S7a and b<sup>†</sup>) with a thickness of around 200 μm (Fig. S7c–e<sup>†</sup>) is introduced between the Li anode and the GPEs. To evaluate the effect of the CNT interlayer in suppressing Li dendrite growth, the Li–Li symmetric cells assembled with bare Li and Li/CNT are evaluated and the configuration is shown in Fig. 3a. Fig. 3b exhibits the plating/stripping behavior of Li/CNT and bare Li at a current density of  $1 \text{ mA cm}^{-2}$  (charge/discharge time: 1 h). After activation in the first few cycles, the cell assembled with bare Li exhibited an overpotential of around 185 mV due to mass-transfer resistance. Intermittent short-circuiting after 110 h and complete short-circuiting after 120 h are observed, which can be attributed to the poor mechanical properties of the GPE as well as non-uniform Li deposition. In contrast, the cell assembled with Li/CNT showed excellent cycling stability, where the overpotential was kept at 71 mV for 800 h of stripping and plating. When further increasing the current density to  $3 \text{ mA cm}^{-2}$  (charge/discharge time: 1 h), the overpotentials of the bare Li and Li/CNT cells both increased to 500 mV and 290 mV, respectively (Fig. 3c). Due to the more serious Li dendrite growth at high current densities and high areal capacities, the cell assembled with bare Li was only able to stably run for 37 h. After that, the

overpotential was sharply reduced to around 0 V and a short circuit was observed. Promisingly, the cell assembled with Li/CNT achieved stable plating/stripping performance at an elevated current density of  $3 \text{ mA cm}^{-2}$  for 400 h with an overpotential that slightly increased to 400 mV. The excellent electrochemical performance of the Li–Li symmetric cells demonstrated the potential to enable high loading QSSLSEBs with excellent electrochemical performance.

To understand the effects of the 3D-printed CNT interlayer during plating/stripping, the Li–Li symmetrical cells operated at a current density of  $1 \text{ mA cm}^{-2}$  were disassembled and the morphology of Li anodes was characterized by SEM. As can be seen from Fig. S8a and b,<sup>†</sup> in the first plating, Li deposited on the bare Li surface exhibited a mossy-like morphology, which can be attributed to the inhomogeneous nucleation and growth.<sup>41</sup> In contrast, no mossy-like or dendritic Li was observed and a smooth surface was obtained on the Li/CNT anode (Fig. S8c and d<sup>†</sup>), enabling desirable uniform charge distribution *via* the CNT interlayer.<sup>42,43</sup> The difference between the two anodes enlarged during the long-term cycling. After 121 h, a fragile and mossy Li layer was detected on the surface of the bare Li and the thickness is 55 μm (Fig. S9a–c<sup>†</sup>). Mossy Li layers are the main cause of low Coulombic Efficiency (CE) and major safety risks in lithium batteries. In comparison with bare Li, the corrosion of the Li anode is significantly reduced with the assistance of the CNT interlayer. The thickness of the mossy Li

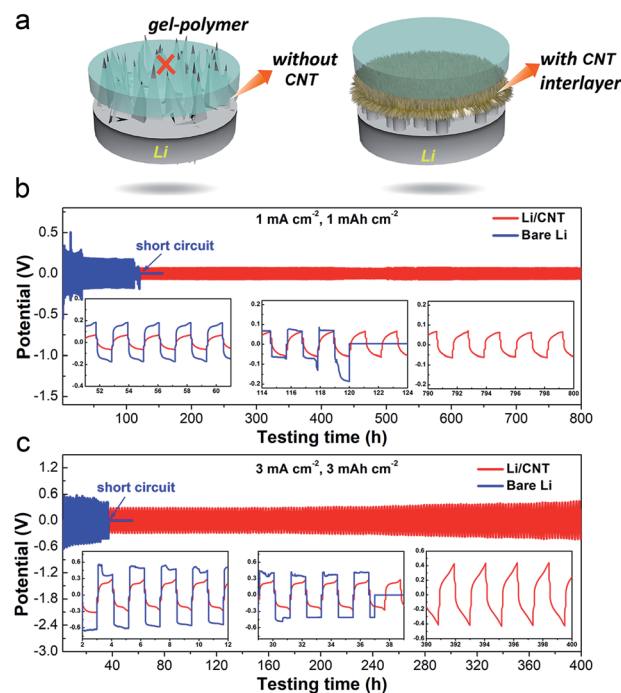


Fig. 3 (a) Schematic diagrams of 3D printing CNTs as an interlayer (named CNT) for protecting Li metal. Galvanostatic discharge/charge voltage profiles of bare Li and CNT/Li electrodes in symmetric coin cells at (b)  $1 \text{ mA cm}^{-2}$  and (c)  $3 \text{ mA cm}^{-2}$  with a stripping/plating capacity of  $1 \text{ mA h cm}^{-2}$  and  $3 \text{ mA h cm}^{-2}$  for 400 cycles and 200 cycles, respectively. The inset graphs in (b) and (c) are enlarged typical profiles of bare Li and Li/CNT electrodes.

layer is around  $20\ \mu\text{m}$  (Fig. S9d–f†), about  $1/3$  that of the bare Li. It can be thus inferred that the printed CNT interlayer is beneficial for enabling uniform charge distribution, preventing Li corrosion and Li dendrite formation. Hence, a better electrochemical performance of QSSLSEBs is realizable.

The different Li deposition behaviors with and without the printed CNT interlayer were verified by the electrochemical performance of QSSLSEBs with 3DPSe- $x$  as the cathodes. The cycling performances of QSSLSEBs assembled with bare Li and Li/CNT anodes, labeled Li|GPE|3DPSe- $x$  and Li/CNT|GPE|3DPSe- $x$ , respectively, were tested at a galvanostatic current density of  $1\ \text{mA}\ \text{cm}^{-2}$  in the voltage range of 0.8–3 V. As exhibited in Fig. 4a, both of the cells with a Se loading of  $4\ \text{mg}\ \text{cm}^{-2}$  delivered a high initial capacity of around  $654\ \text{mA}\ \text{h}\ \text{g}^{-1}$  and retained a reversible capacity of around  $600\ \text{mA}\ \text{h}\ \text{g}^{-1}$  in the second cycle. It should be noted that the Li/CNT|GPE|3DPSe-4 cell maintained high and stable CEs of around 100% within 200 cycles, while the CE of the

Li|GPE|3DPSe-4 cell suddenly dropped to around 30% in the 5<sup>th</sup> cycle from 100% in the 4<sup>th</sup> cycle. As the electrolyte and cathode were identical in the two cells, the dramatic difference in CE can be attributed to the different anodes in the two cells. Although at a high capacity of  $650.0\ \text{mA}\ \text{h}\ \text{g}^{-1}$ , corresponding to an areal capacity of  $2.6\ \text{mA}\ \text{h}\ \text{cm}^{-2}$ , as delivered by the Li|GPE|3DPSe-4 cell, the GPE was not able to meet the demand for suppressing the Li dendrite growth, as illustrated by the Li–Li symmetrical cells. In this regard, a short circuit occurs, which is demonstrated by the charge/discharge profiles in Fig. S10.† In contrast, the Li/CNT|GPE|3DPSe-4 cell retained high CEs of around 100% during the whole charge/discharge process as shown in Fig. 4b. A high capacity of  $538.1\ \text{mA}\ \text{h}\ \text{g}^{-1}$  was retained after 200 cycles, corresponding to a capacity attenuation of 0.042% from  $585.9\ \text{mA}\ \text{h}\ \text{g}^{-1}$  (5<sup>th</sup> cycles) to  $538.1\ \text{mA}\ \text{h}\ \text{g}^{-1}$  (200<sup>th</sup> cycles), which further confirmed the strong capability of the CNT interlayer in suppressing Li dendrite growth. In order to further demonstrate

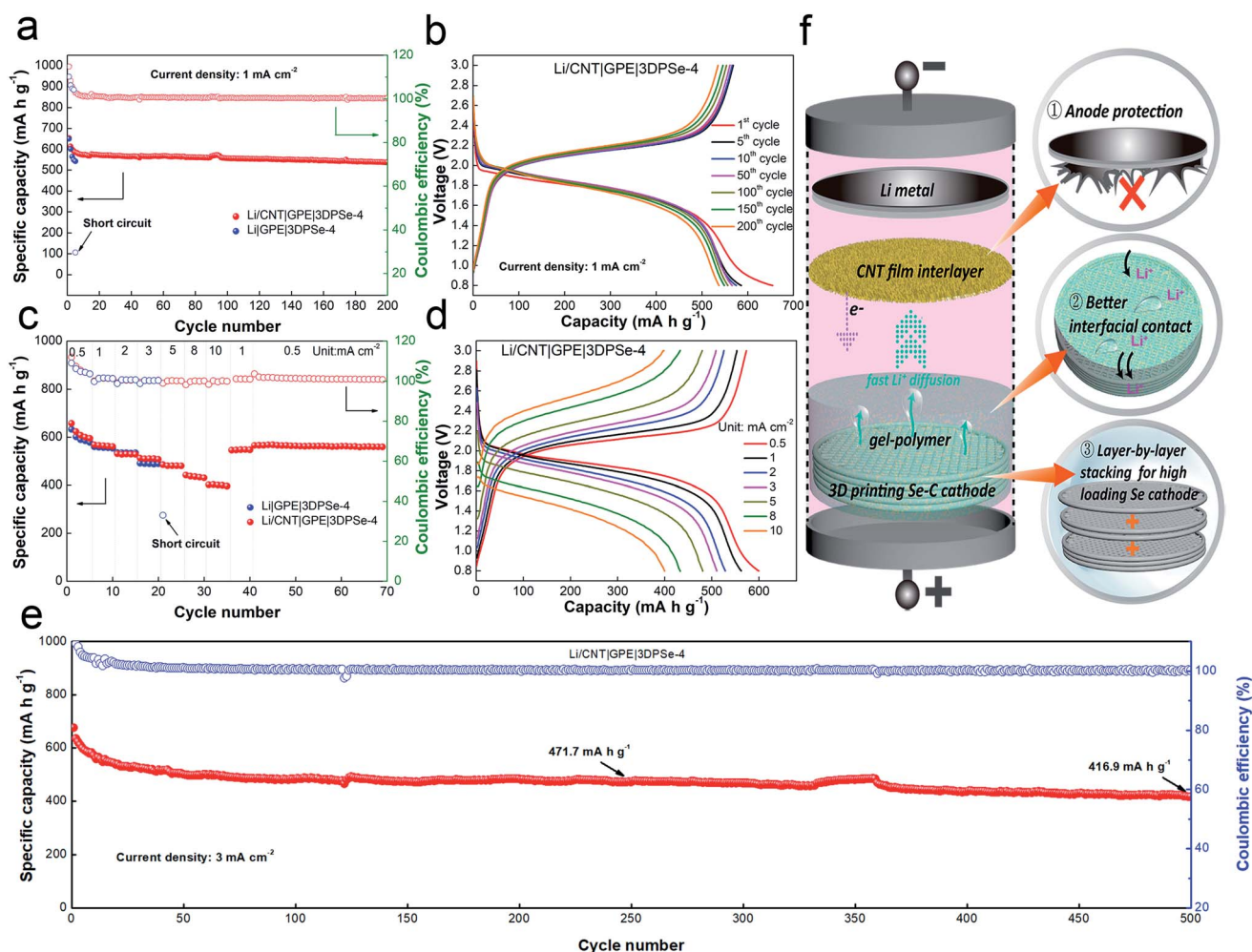


Fig. 4 Electrochemical performance of QSSLSEBs with the 3DPSe-4 cathodes (Li/CNT|GPE|3DPSe-4 and Li|GPE|3DPSe-4). (a) Cycling performance at a current density of  $1\ \text{mA}\ \text{cm}^{-2}$  and corresponding CEs. (b) Discharge/charge voltage profile of Li/CNT|GPE|3DPSe-4 at a current density of  $1\ \text{mA}\ \text{cm}^{-2}$ . (c) Rate performance at current densities ranging from  $0.5\ \text{mA}\ \text{cm}^{-2}$  to  $10\ \text{mA}\ \text{cm}^{-2}$  and corresponding CEs. (d) Discharge/charge profiles of Li/CNT|GPE|3DPSe-4 at different current densities ranging from  $0.5\ \text{mA}\ \text{cm}^{-2}$  to  $10\ \text{mA}\ \text{cm}^{-2}$ . (e) Long-term cycling performance of Li/CNT|GPE|3DPSe-4 at a current density of  $3\ \text{mA}\ \text{cm}^{-2}$ . (f) Schematic illustration of the 3DPSe- $x$  cathode for promoting  $\text{Li}^+$  immigration in a QSSLSEB model.

the Li dendrite suppression capability of the CNT interlayer, the rate performance of Li/CNT|GPE|3DPSe-4 and Li|GPE|3DPSe-4 cells was determined at various current densities from 0.5 mA cm<sup>-2</sup> to 10 mA cm<sup>-2</sup> (Fig. 4c). The Li/CNT|GPE|3DPSe-4 cell delivered average reversible capacities of 657.7, 568.3, 531, 512.4, 485.1, 441.6, and 401.9 mA h g<sup>-1</sup> at current densities of 0.5, 1, 2, 3, 5, 8, and 10 mA cm<sup>-2</sup>, respectively, corresponding well with charge and discharge profiles shown in Fig. 4d. More importantly, when the current densities were reset to 1 and 0.5 mA cm<sup>-2</sup>, the cell could still retain capacities of 545.7 and 565.6 mA h g<sup>-1</sup>, demonstrating the good reversibility of Li/CNT|GPE|3DPSe-4. In contrast, the Li|GPE|3DPSe-4|GP cell delivered similar rate performance from 0.5 to 3 mA cm<sup>-2</sup>. However, it should be noted that a sudden drop of CE was observed at 3 mA cm<sup>-2</sup>, indicating a short-circuit (Fig. 4c). The long-term cycling performance of the Li/CNT|GPE|3DPSe-4/GP cell was also investigated at a current density of 3 mA cm<sup>-2</sup>, as shown in Fig. 4e, which demonstrated a capacity of 416.9 mA h g<sup>-1</sup> over 500 cycles. The improved reversibility and stability of Li/CNT|GPE|3DPSe-4/GP battery is illustrated in Fig. 4f. From a mechanism standpoint, first, Li dendrite growth was effectively suppressed by the 3D printed CNT interlayer. Second, the combination of 3DPSe cathode host and GPEs enabled close contact between the GPE and the Se/C cathode, reducing the interfacial resistance. Third, the 3DPSe cathode with GPEs infusion facilitated the Li<sup>+</sup> migration, which ensured high Se utilization and high rate performance as well. To confirm the

improvement of Li<sup>+</sup> transport in the 3DPSe cathodes, Se cathodes were fabricated *via* a blade casting method and labeled as BCSe-*x* (*x* is the Se loading), for comparison. As shown in Fig. S11,† taking BCSe-10 as an example, these cathodes exhibited a dense structure accompanied by many surface cracks, which is harmful for both Li<sup>+</sup> and e<sup>-</sup> transport during the charging/discharging process. The electrochemical impedance spectroscopy (EIS) curves of the QSSLSEBs assembled with 3DPSe-*x* and BCSe-*x* cathodes are shown in Fig. S12† and relative simulation results are listed in Table S1.† To further quantify the difference of Li<sup>+</sup> diffusion in 3DPSe-*x* cathodes and BCSe-*x* counterparts, the diffusion coefficient of Li<sup>+</sup> ( $D_{Li^+}$ ) was calculated based on the  $D_{Li^+}$ -Warburg coefficient ( $\sigma$ )-angular frequency ( $\omega$ ) relationships as previously reported.<sup>44,45</sup> Fig. S12c and d† demonstrate that the 3DPSe-*x* cathodes have a similar  $D_{Li^+}$ ,  $5.0 \times 10^{-10}$  cm<sup>2</sup> s<sup>-1</sup>, which is almost 50 times that of the BCSe-4 cathode ( $9.77 \times 10^{-12}$  cm<sup>2</sup> s<sup>-1</sup>) and 500 times that of BCSe-10 ( $1.38 \times 10^{-12}$  cm<sup>2</sup> s<sup>-1</sup>) and BCSe-20 ( $1.04 \times 10^{-12}$  cm<sup>2</sup> s<sup>-1</sup>) cathodes. The 3DPSe-*x* cathodes possess smaller charge transfer resistance ( $R_{ct}$ ) and larger  $D_{Li^+}$ , suggesting higher electrochemical activity and faster Li<sup>+</sup> diffusion.<sup>46</sup> The above results further highlighted the unique structure of 3DPSe-*x* with GPE infusion for facilitating Li<sup>+</sup> transport in the thick Se electrodes.

To further confirm the concepts above, the electrochemical performance of a high Se-loading QSSLSEB assembled with both 3DPSe-*x* and BCSe-*x* (*x* = 10 and 20) electrodes was investigated, as shown in Fig. 5 and S13.† The Li/

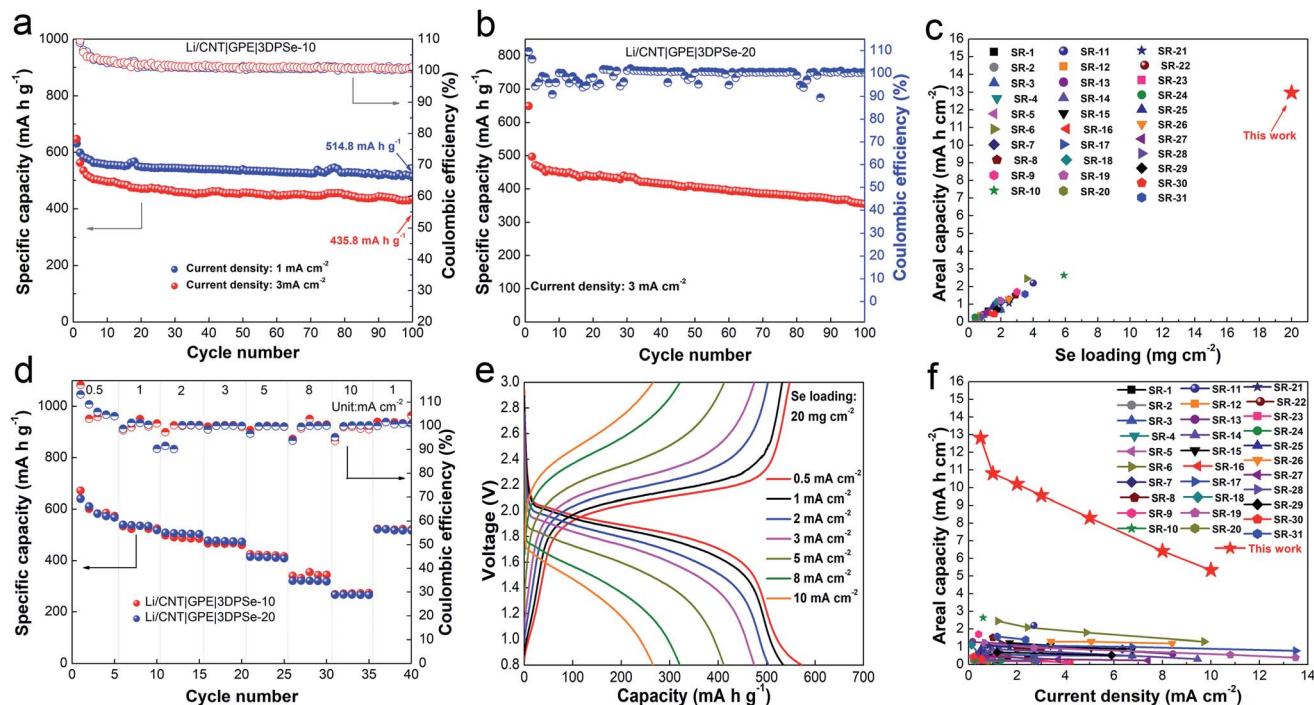


Fig. 5 Cycling performance of a full cell of Li/CNT|GPE|3DPSe-*x* (*x* is 10 and 20). (a) Cycling performance of Li/CNT|GPE|3DPSe-10 at current densities of 1 mA cm<sup>-2</sup> and 3 mA cm<sup>-2</sup> for 100 cycles. (b) Cycling performance of Li/CNT|GPE|3DPSe-20 at a current density of 3 mA cm<sup>-2</sup>. (c) Comparison of areal capacity based on Se loading in publications from recent 6 years and our reports on Li-Se batteries. (d) Rate capability curves of Li/CNT|GPE|3DPSe-*x* (*x* is 10 and 20) at various densities from 0.5 mA cm<sup>-2</sup> to 10 mA cm<sup>-2</sup>. (e) Galvanostatic discharge and charge curves of Li/CNT|GPE|3DPSe-20 at various densities from 0.5 mA cm<sup>-2</sup> to 10 mA cm<sup>-2</sup>. (f) Comparison of areal capacity based on different current densities with studies in recent 6 years on Li-Se batteries.

CNT|GPE|3DPSe-10 cell exhibited a high initial discharge capacity of around  $640 \text{ mA h g}^{-1}$ , corresponding to an areal capacity of  $6.4 \text{ mA h cm}^{-2}$ , and retained capacities of over  $514.8$  and  $435.8 \text{ mA h g}^{-1}$  after 100 cycles operating at current densities of  $1$  and  $3 \text{ mA cm}^{-2}$ , respectively, as shown in Fig. 5a. The relative charge/discharge profiles of the Li/CNT|GPE|3DPSe-10 cell at a current density of  $3 \text{ mA cm}^{-2}$  are provided in Fig. S13,† demonstrating excellent cycling stability and low overpotentials during cycling. In contrast, the capacity of Li/CNT|GPE|BCSe-10 dropped rapidly, even to near  $0 \text{ mA h g}^{-1}$  after 100 cycles at  $3 \text{ mA cm}^{-2}$  (Fig. S14a and b†). In order to clarify the reasons leading to the huge difference, both QSSLSEBs assembled with BCSe-10 and 3DPSe-10 electrodes were disassembled after cycling, as illustrated in Fig. S15.† It was found that all electrode materials could easily peel off from the current collector of the BCSe-10 electrode and resulted in active material loss. Interestingly, the 3DPSe-10 electrode maintained its structure well during cycling, which was confirmed by the optical images in Fig. S15c.† Hence, we conclude that the 3DPSe-*x* electrodes possess high structural stability as well as fast  $\text{Li}^+$  transport capability, attributed to the improved cycling stability and rate performance for the high loading QSSLSEBs. Moreover, QSSLSEBs assembled with an ultrahigh Se-loading of  $20 \text{ mg cm}^{-2}$  were investigated at current densities of  $1$  and  $3 \text{ mA cm}^{-2}$  to achieve higher energy densities. To deeply understand the excellent cycling stability of the QSSLSEBs, the structure of 3DPSe-10 before and after cycling is characterized by XRD. As shown in Fig. S16,† it can be found that only carbon peaks can be detected, suggesting that the Se species are confined well in the BP2000 carbon during cycling. As shown in Fig. S17† and 5b, both cells delivered a high initial capacity of around  $649 \text{ mA h g}^{-1}$ , equaling a high areal capacity of  $12.99 \text{ mA h cm}^{-2}$ . To the best of our knowledge, both the Se loading and areal capacity are the highest. Compared with recent publications, such a high areal capacity is at least 4 times higher than that of most of the reported state-of-the-art conventional Li–Se batteries that we listed in Fig. 5c and Table S2.† More significantly, high discharge capacities of  $484.6$  and  $354.5 \text{ mA h g}^{-1}$  were retained after 50 and 100 cycles, respectively, demonstrating excellent cycling performance. Furthermore, the rate performance of Li/CNT|GPE|3DPSe-10 and Li/CNT|GPE|3DPSe-20 cells was investigated, as seen in Fig. 5d, which delivered similar reversible capacities at current densities of  $0.5, 1, 2, 3, 5,$  and  $8 \text{ mA cm}^{-2}$ , respectively. Even at an ultrahigh current density of  $10 \text{ mA cm}^{-2}$ , a high capacity of about  $270 \text{ mA h g}^{-1}$  was still retained, corresponding well with Fig. 5e. When the current densities were returned to  $1$  and  $0.5 \text{ mA cm}^{-2}$ , the capacity of these two cells could recover to around  $524 \text{ mA h g}^{-1}$ , suggesting reversible electrochemical behavior and high stability of 3DPSe-10 and 3DPSe-20 electrodes at high current densities. Compared with the Li/CNT|GPE|3DPSe-10 cell, the Li/CNT|GPE|BCSe-10 cell exhibited worse rate performance and fast capacity decay when the current densities were higher than  $3 \text{ mA cm}^{-2}$ . This is mainly attributed to the low  $\text{Li}^+$  transport in the BCSe-10 cell, which was not able to meet the requirements of  $\text{Li}^+$  diffusion at high current densities. From the charge/discharge profiles in Fig. S14d,† we confirmed that

the overpotential increased sharply at higher current densities over  $3 \text{ mA cm}^{-2}$ . However, the charge/discharge profiles of the Li/CNT|GPE|3DPSe-20 cell at different current densities shown in Fig. 5e shows a lower overpotential compared with that of the Li/CNT|GPE|BCSe-10 cell.

All the results coincided well with the aforementioned EIS results and further highlighted the merits of 3DPSe-*x* electrodes. This excellent rate capability of the Li/CNT|GPE|3DPSe-20 cell were compared with previous studies related to Li–Se batteries in recent publications as shown in Fig. 5f. From the comparison, this work demonstrated the highest areal capacity at higher current densities. To further confirm that the structure of QSSLSEBs designed in this work is also suitable for high Se content cathodes, Se/C composites with a Se content of 70% are also synthesized and then Se/C composites were printed, named as 3DPSe-*x* cathode (*x* are 4 and  $10 \text{ mg cm}^{-2}$ ) to test their electrochemical performance. As shown in Fig. S18,† the TGA curve demonstrates that the Se content in the Se/C composite is 70 wt%. The electrochemical performance of the Li/CNT|GPE|3DPSe-*x* cell with Se loadings of 4 and  $10 \text{ mg cm}^{-2}$  is shown in Fig. S19 and S20.† It also demonstrates excellent cycling stability with high capacities of  $442.9$  ( $4 \text{ mg cm}^{-2}$ ) and  $469 \text{ mA h g}^{-1}$  ( $10 \text{ mg cm}^{-2}$ ) after 100 and 30 cycles at a current density of  $3 \text{ mA cm}^{-2}$ , respectively. These results further show the novelty of this work, which is focused on 3D-printing quasi-solid-state Li–Se batteries by combining a gel polymer and high-Se loading cathodes.

## Conclusions

In summary, we developed a high energy/power-density QSSLSEB by combining a 3D-printed CNT interlayer and GPE filled 3DPSe-*x* cathodes. The CNT interlayer is beneficial for Li dendrite suppression, enabling the Li–Li symmetric cell to stably run for 400 h at a current density of  $3 \text{ mA cm}^{-2}$  and an areal capacity of  $3 \text{ mA h cm}^{-2}$ , which is almost 10 times longer compared with the interlayer-free cell. Additionally, the 3DPSe cathodes with a grid structure provide large spaces for GPE impregnation to build interconnected  $\text{Li}^+$  transport channels in thick electrodes, enabling fast  $\text{Li}^+$  transport in QSSLSEBs. Accordingly, the Li/CNT|GPE|3DPSe-*x* QSSLSEB exhibits excellent cycling stability and remarkable rate performance with high Se loadings of 4– $20 \text{ mg cm}^{-2}$ . The QSSLSEBs assembled with the 3DPSe-10 cathode delivers a specific capacity of  $435.8 \text{ mA h g}^{-1}$  at a high current density of  $3 \text{ mA cm}^{-2}$  after 100 cycles. Moreover, with an ultrahigh Se loading of  $20 \text{ mg cm}^{-2}$ , the QSSLSEB delivers the highest reported areal capacity of  $12.99 \text{ mA h cm}^{-2}$  at a high current density of  $3 \text{ mA cm}^{-2}$ . We believe that this achievement will generate substantial interest and shed light on the R&D of other solid-state energy storage systems such as Li–S, Li-ion and Na-ion batteries.

## Statement of contributions

X. Gao and X. Yang contributed equally to this work. They conceived the idea and designed the experiments. X. Sun and T.-K. Sham as supervisors gave guidance and support to the

project. Q. Sun helped design and discussed the experiments. S. Wang designed and drew the schematic. R. Li assisted with characterization. C. Zhao and J. Liang did the Scanning Electron Microscopy (SEM) and thermogravimetric analysis (TGA) characterization, respectively. Y. Zhao assisted with analysing Li symmetric data. M. Zheng and J. Wang designed the 3D printing process for printing the electrodes. X. Li and M. Li assisted with analysing the EIS curves. X. Gao wrote the manuscript. All authors discussed the results and commented on the manuscript.

## Conflicts of interest

There are no conflicts to declare.

## Acknowledgements

This work was partly supported by the Natural Sciences and Engineering Research Council of Canada (NSERC), Canada Research Chair Program (CRC), China Automotive Battery Research Institute, Ontario Research Fund, Canada Foundation for Innovation (CFI), and Western University.

## Notes and references

- Q. Pang, A. Shyamsunder, B. Narayanan, C. Y. Kwok, L. A. Curtiss and L. F. Nazar, *Nat. Energy*, 2018, **3**, 783–791.
- R. Fang, S. Zhao, P. Hou, M. Cheng, S. Wang, H. M. Cheng, C. Liu and F. Li, *Adv. Mater.*, 2016, **28**, 3374–3382.
- Q. Pang, C. Y. Kwok, D. Kundu, X. Liang and L. F. Nazar, *Joule*, 2019, **3**, 136–148.
- L. Peng, P. Xiong, L. Ma, Y. Yuan, Y. Zhu, D. Chen, X. Luo, J. Lu, K. Amine and G. Yu, *Nat. Commun.*, 2017, **8**, 15139.
- C. Hu, Y. Xiao, Y. Zou and L. Dai, *Electrochem. Energy Rev.*, 2018, **1**, 84–112.
- X. Ji, K. T. Lee and L. F. Nazar, *Nat. Mater.*, 2009, **8**, 500–506.
- X. Yang, H. Zhang, Y. Chen, Y. Yu, X. Li and H. Zhang, *Nano Energy*, 2017, **39**, 418–428.
- Y. Dong, S. Zheng, J. Qin, X. Zhao, H. Shi, X. Wang, J. Chen and Z.-S. Wu, *ACS Nano*, 2018, **12**, 2381–2388.
- L. Luo, S.-H. Chung and A. Manthiram, *Adv. Energy Mater.*, 2018, **8**, 1801014.
- A. Manthiram, Y. Fu, S. H. Chung, C. Zu and Y. S. Su, *Chem. Rev.*, 2014, **114**, 11751–11787.
- J. Zhou, X. Liu, L. Zhu, J. Zhou, Y. Guan, L. Chen, S. Niu, J. Cai, D. Sun, Y. Zhu, J. Du, G. Wang and Y. Qian, *Joule*, 2018, **2**, 2681–2693.
- R. Xu, T. Wu, J. Lu and K. Amine, *Li-S Batteries: The Challenges, Chemistry, Materials, and Future Perspectives*, 2017, p. 309.
- Q. Cai, Y. Li, Q. Li, J. Xu, B. Gao, X. Zhang, K. Huo and P. K. Chu, *Nano Energy*, 2017, **32**, 1–9.
- H. Lv, R. Chen, X. Wang, Y. Hu, Y. Wang, T. Chen, L. Ma, G. Zhu, J. Liang and Z. Tie, *ACS Appl. Mater. Interfaces*, 2017, **9**, 25232–25238.
- L.-C. Zeng, W.-H. Li, Y. Jiang and Y. Yu, *Rare Met.*, 2017, **36**, 339–364.
- X. Zhao, L. Yin, T. Zhang, M. Zhang, Z. Fang, C. Wang, Y. Wei, G. Chen, D. Zhang, Z. Sun and F. Li, *Nano Energy*, 2018, **49**, 137–146.
- Y. Cui, A. Abouimrane, J. Lu, T. Bolin, Y. Ren, W. Weng, C. Sun, V. A. Maroni, S. M. Heald and K. Amine, *J. Am. Chem. Soc.*, 2013, **135**, 8047–8056.
- D. B. Babu and K. Ramesha, *Electrochim. Acta*, 2016, **219**, 295–304.
- Z. Li, L. Yuan, Z. Yi, Y. Liu and Y. Huang, *Nano Energy*, 2014, **9**, 229–236.
- J. He, Y. Chen, W. Lv, K. Wen, P. Li, Z. Wang, W. Zhang, W. Qin and W. He, *ACS Energy Lett.*, 2016, **1**, 16–20.
- L. Zeng, W. Zeng, Y. Jiang, X. Wei, W. Li, C. Yang, Y. Zhu and Y. Yu, *Adv. Energy Mater.*, 2015, **5**, 1401377.
- L. Zeng, X. Wei, J. Wang, Y. Jiang, W. Li and Y. Yu, *J. Power Sources*, 2015, **281**, 461–469.
- G. L. Xu, H. Sun, C. Luo, L. Estevez, M. Zhuang, H. Gao, R. Amine, H. Wang, X. Zhang and C. J. Sun, *Adv. Energy Mater.*, 2019, **9**, 1802235.
- A. Manthiram, X. Yu and S. Wang, *Nat. Rev. Mater.*, 2017, **2**, 16103.
- Y. Zhang, Y. Sun, L. Peng, J. Yang, H. Jia, Z. Zhang, B. Shan and J. Xie, *Energy Storage Mater.*, 2019, **21**, 287–296.
- K. H. Park, Q. Bai, D. H. Kim, D. Y. Oh, Y. Zhu, Y. Mo and Y. S. Jung, *Adv. Energy Mater.*, 2018, **8**, 1800035.
- X. Li, J. Liang, X. Li, C. Wang, J. Luo, R. Li and X. Sun, *Energy Environ. Sci.*, 2018, **11**, 2828–2832.
- X. Li, J. Liang, J. Luo, C. Wang, X. Li, Q. Sun, R. Li, L. Zhang, R. Yang and S. Lu, *Adv. Mater.*, 2019, **31**, 1808100.
- J. Zhou, H. Ji, J. Liu, T. Qian and C. Yan, *Energy Storage Mater.*, 2019, **22**, 256–264.
- X. Cheng, J. Pan, Y. Zhao, M. Liao and H. Peng, *Adv. Energy Mater.*, 2018, **8**, 1702184.
- B. Liu, Y. Gong, K. Fu, X. Han, Y. Yao, G. Pastel, C. Yang, H. Xie, E. D. Wachsman and L. Hu, *ACS Appl. Mater. Interfaces*, 2017, **9**, 18809–18815.
- M. Zhu, J. Wu, W. H. Zhong, J. Lan, G. Sui and X. Yang, *Adv. Energy Mater.*, 2018, **8**, 1702561.
- T. S. Wei, B. Y. Ahn, J. Grotto and J. A. Lewis, *Adv. Mater.*, 2018, **30**, 1703027.
- X. Gao, Q. Sun, X. Yang, J. Liang, A. Koo, W. Li, J. Liang, J. Wang, R. Li and F. B. Holness, *Nano Energy*, 2019, **56**, 595–603.
- J. Wang, Q. Sun, X. Gao, C. Wang, W. Li, F. B. Holness, M. Zheng, R. Li, A. D. Price and X. Sun, *ACS Appl. Mater. Interfaces*, 2018, **10**, 39794–39801.
- K.-H. Choi, J. Yoo, C. K. Lee and S.-Y. Lee, *Energy Environ. Sci.*, 2016, **9**, 2812–2821.
- S.-H. Kim, K.-H. Choi, S.-J. Cho, J. Yoo, S.-S. Lee and S.-Y. Lee, *Energy Environ. Sci.*, 2018, **11**, 321–330.
- L. Sha, P. Gao, X. Ren, Q. Chi, Y. Chen and P. Yang, *Chem.–Eur. J.*, 2018, **24**, 2151–2156.
- R. Mukkabla, K. Wadhwa and M. Deepa, *ACS Appl. Energy Mater.*, 2018, **1**, 6964–6976.
- X. Yang, Y. Chen, M. Wang, H. Zhang, X. Li and H. Zhang, *Adv. Funct. Mater.*, 2016, **26**, 8427–8434.

- 41 C. Zhao, J. Liang, Q. Sun, J. Luo, Y. Liu, X. Lin, Y. Zhao, H. Yadegari, M. N. Bani, R. Li, H. Huang, L. Zhang, R. Yang, S. Lu and X. Sun, *Small Methods*, 2018, 1800437.
- 42 Q. Li, S. Zhu and Y. Lu, *Adv. Funct. Mater.*, 2017, 27, 1606422.
- 43 Y. Zhao, Q. Sun, X. Li, C. Wang, Y. Sun, K. R. Adair, R. Li and X. Sun, *Nano Energy*, 2018, 43, 368–375.
- 44 X. Gao, X. Yang, M. Li, Q. Sun, J. Liang, J. Luo, J. Wang, W. Li, J. Liang and Y. Liu, *Adv. Funct. Mater.*, 2019, 29, 1806724.
- 45 X. Yang, X. Gao, Q. Sun, S. P. Jand, Y. Yu, Y. Zhao, X. Li, K. Adair, L. Y. Kuo and J. Rohrer, *Adv. Mater.*, 2019, 31, 1901220.
- 46 X. Yang, Q. Sun, C. Zhao, X. Gao, K. Adair, Y. Zhao, J. Luo, X. Lin, J. Liang and H. Huang, *Energy Storage Materials*, 2019, 61, 567–575.